

WiRM: Wireless Respiration Monitoring Using Conjugate Multiple Channel State Information and Fast Iterative Filtering in Wi-Fi Systems

James Rhodes, Lawrence Ong, and Duy T. Ngo



Abstract—Monitoring respiratory health with the use of channel state information (CSI) has shown promising results. Many existing methods focus on monitoring only the respiratory rate, while others focus on monitoring the motion of the chest as a patient breathes, which is referred to as the *respiratory waveform*. This paper presents WiRM, a two-staged approach to contactless respiration monitoring. In the first stage, WiRM improves upon existing respiratory rate estimation techniques by using conjugate multiplication for phase sanitisation and adaptive multi-trace carving (AMTC) for tracing how the respiratory rate changes over time. When compared against three state-of-the-art methods, WiRM has achieved an average reduction of 38% in respiratory rate root mean squared error (RMSE). In the second stage, WiRM uses this improved respiratory rate estimate to inform the decomposition and selection of the respiratory waveform from the CSI data. Remarkably, WiRM delivers a 178.3% improvement in average absolute correlation with the ground truth respiratory waveform. Within the literature, it is difficult to compare the robustness of existing algorithms in noisy environments. In this paper, we develop a purpose-built simulation toolkit to evaluate the robustness of respiration monitoring solutions under various noise conditions, including thermal, multiplicative, and phase noise. Our results show that WiRM demonstrates improved or comparable resilience to these common noise sources.

Index Terms—Adaptive multi-trace carving, channel state information, conjugate multiplication, fast iterative filtering, integrated sensing and communication, respiration monitoring

1 INTRODUCTION

RESPIRATION monitoring is a key diagnostic tool utilised by medical practitioners to monitor a patient's health. The monitoring of respiratory health can include a patient's respiratory rate or the motion of the patient's chest in a direction normal to the torso as they breathe, referred to as the *respiratory waveform*. The accurate tracking of both the respiratory rate and the respiratory waveform can aid in the diagnosis of many illnesses.

The gold standard methodology for monitoring respiratory rate in hospitals is for a healthcare worker to manually

count the number of inhalations over one-minute periods [1]. This is time-consuming for patients and professionals, introducing human error into the monitoring. The state-of-the-art automatic respiratory rate monitoring, e.g., during a polysomnography test, requires patients to wear several uncomfortable pieces of equipment such as a belt to monitor the motion of the chest and/or pressure transducers to monitor the breath. This can cause discomfort to the patients, potentially skewing the results of sleep tests.

Similar to the measurement of respiratory rate, the respiratory waveform is commonly measured manually or via uncomfortable equipment. Unlike respiratory rate which provides a single scalar value, the respiratory waveform captures the full temporal dynamics of breathing. This richer signal enables a broader range of diagnostic applications, including monitoring airflow and volume changes, identifying apnoea, and identifying abnormal chest wall movements [2]. These capabilities make the waveform more informative than respiratory rate alone, the latter of which can often be readily derived from the waveform.

While optical methods for contactless respiration monitoring aim to solve the discomfort problem, the need for constant visual surveillance of a patient incurs privacy concerns. The need for a respiratory rate monitoring solution that is cost-effective, privacy-preserving, contactless, and automated is therefore apparent.

Wireless technologies provide an opportunity for contactless sensing of motion and, by not using cameras, offer a more private experience for patients. Wireless respiratory rate monitoring is an active area of research with advancements utilising acoustics [3], [4], Radio Frequency Identification (RFID) [5], [6], radar [7], [8], and commodity Wi-Fi [9], [10]. Except for Wi-Fi, all of these methods require specialised equipment such as microphones, RFID tags, or costly radar systems. This makes Wi-Fi-based approaches stand out thanks to the low cost and proliferation of Wi-Fi systems in homes and public spaces.

Existing Wi-Fi-based methods for estimating respiratory rate and waveforms, however, have their shortcomings. Direct respiratory rate estimation continues to struggle in environments with a low signal-to-noise ratio and does not provide medical practitioners with a respiratory waveform for diagnostic purposes [11], [12]. Methods that compute the waveform directly are generally more sensitive to noise.

This work has been submitted to the IEEE for possible publication. Copyright may be transferred without notice, after which this version may no longer be accessible.

James Rhodes, Lawrence Ong, and Duy T. Ngo are with the School of Engineering, The University of Newcastle, Australia (e-mail: j.rhodes@uon.edu.au, lawrence.ong@newcastle.edu.au, duy.ngo@newcastle.edu.au).

This work is supported in part by The University of Newcastle through an Australian Government Research Training Program Scholarship (Strategic Engagement Scheme).

They also employ decomposition techniques that require an additional, usually heuristic-based, method to extract the breath signal from the set of decomposed signals [13]. Furthermore, since there is a severe lack of datasets or simulation methods in this area of research, different sources of data are being used, making it challenging to compare the performance of different methods.

This paper proposes a novel Wireless Respiration Monitoring (WiRM) solution to address the above issues. Specifically:

- **WiRM – Stage 1:** We first propose a new respiratory rate estimation algorithm that utilises adaptive multi-trace carving with an empirically determined respiratory rate transition probability function. The aim is to improve respiratory rate tracking performance. Our proposed rate estimation algorithm demonstrates an improvement of 38% in average Root Mean Square Error (RMSE) compared to the state-of-the-art techniques.
- **WiRM – Stage 2:** We then propose a new method for estimating respiratory waveforms from previous respiratory rate estimations, utilising the fast iterative filtering algorithm. Our proposed waveform estimation method delivers an improvement of 178.3% in average absolute correlation and 55.4% in maximum absolute correlation over the state-of-the-art techniques.
- **Simulation Toolkit and Performance Evaluation in Noisy Environments:** We develop a purpose-built simulation toolkit to systematically evaluate the performance of our proposed WiRM algorithm against ideal CSI models under three common noise sources: thermal, multiplicative, and phase. Numerical results with practical parameter settings show that WiRM demonstrates substantial robustness across all three noise types, consistently matching or exceeding the performance of existing leading algorithms.

2 RELATED WORKS

The first advances in Wi-Fi-based sensing use received signal strength as an indicator of various movements within the environment [14]. The use of signal power was not fine-grained enough for more advanced use cases of sensing. To overcome this granularity problem, researchers turn to utilising the Wi-Fi’s channel state information (CSI).

Some key application domains enabled by CSI’s fine-grained measurements include fall-detection [15], human activity recognition (HAR) [16], gait estimation [17], speed estimation [18], indoor localisation and tracking [19], and vital sign monitoring [20]. All of these research areas aim to address a common problem of detecting minute changes in CSI measurements relating to direct physical movement in the environment.

Changes in the environment are reflected in both the phase and magnitude of the measured CSI. As the phase is often affected by noise, pre-processing or estimation techniques are needed to remove it. The three broad categories of methods for detecting changes in the environment using CSI measurements include using the magnitude of CSI (or similarly, CSI energy) [11], [18], [21], the phase of CSI [16],

[22]–[26], or a combination of both [13], [27], [28] to avoid “blind spots” [29].

2.1 Direct Respiratory Rate Estimation

TR-BREATH is one of the first methods to realise simultaneous, multi-user respiration rate detection. Specifically, it utilises the spatial and temporal focusing effects of the time reversal principle (TR) and time reversal resonating strength (TRRS) to detect minute changes in the environment, allowing for the calculation of the respiratory rate [12]. The TRRS is analogous to a correlation coefficient and accurately describes how the environment changes with time. The TRRS is computed across a time window, followed by applying the Root Multiple Signal Classification (Root-MUSIC) algorithm to gather candidate breathing rates. The output of the Root-MUSIC algorithm is used to compute statistics about the breathing data, which is then fed into a support vector machine to detect whether breath is present or not. The output of the Root-MUSIC algorithm is also used in conjunction with affinity propagation clustering and likelihood assignment to determine the likely breathing rates [12]. As the Root-MUSIC algorithm incurs high computational complexity, TR-BREATH is more suitable for off-line computations.

A competing approach to detecting motion within CSI uses the autocorrelation function (ACF). This approach has motion detection capabilities similar to the TR principle [30] and was first applied to respiration monitoring by SMARS: *Sleep Monitoring via Ambient Radio Signals* [11]. The SMARS method measures the period of breathing based on the distance between the peaks and troughs of the ACF of the CSI energy. While using the ACF allows this method to be executed in real time, its performance is quite sensitive to noise.

Building on SMARS, Wang *et al.* compute an ACF at each time step to construct an ACF spectrum in their study, *WiResP: A Robust Wi-Fi-Based Respiration Monitoring via Spectrum Enhancement* [21]. Image-processing techniques are then applied to the ACF spectrum, which is subsequently compared to a template ACF spectrum known to contain breathing patterns, enhancing breath detection capabilities.

It should be noted that both WiResP and SMARS use only the CSI energy, which has been shown to create “blind spots” within a given room. Due to the phase noise, using both the phase and the magnitude of the CSI does not necessarily solve the blind-spot problem [25]. In this paper, we use conjugate multiplication to cancel out phase noise, enabling the use of both the magnitude and phase of the CSI to address the blind-spot problem [25]. We then apply the ACF to detect the periodic respiratory rate within CSI data as described in Section 4. Independent and concurrent to our research, Wang *et al.* [31] have used conjugate multiplication and the parametric symmetric ACF in a different application, i.e., fall detection.

2.2 Respiratory Waveform Estimation

Methods for extracting the respiratory waveform generally share similar steps. They include pre-processing (such as filtering or smoothing the raw CSI data), signal selection (such as choosing between CSI amplitude, phase, or other

metrics), and a decomposition technique to extract potential breath waveforms, from which the final breath waveform can be determined. Popular decomposition methods include empirical mode decomposition (EMD) [32], independent component analysis [8], [26], [33], canonical polyadic decomposition [23], discrete wavelet transform [24], variational mode decomposition (VMD) [13], [34], and principal component analysis (PCA) [13].

TensorBeat is among the first to realise respiratory-waveform estimation from CSI data [23]. It addresses the phase noise by taking the difference between the phase measured at two antennas on the same network interface card (NIC), referred to as the CSI phase difference. Such data are decomposed by using the canonical polyadic decomposition, where the decomposed signals are grouped and matched to a person with the use of ACF, dynamic time warping, and the stable roommate matching algorithm. Having used only the phase of the CSI, TensorBeat however does not address the blind-spot issue.

Building upon TensorBeat, PhaseBeat also uses the CSI phase difference [24]. PhaseBeat, after performing calibration of the CSI phase difference data, performs a subcarrier selection routine using the mean absolute deviation. The discrete wavelet transform is applied to the selected subcarrier to extract a respiratory waveform. Similar to TensorBeat, the blind-spot issue has not been mitigated within the PhaseBeat algorithm.

Building upon TensorBeat and Phasebeat, Zhuo *et al.* [13] propose using the ratio of the CSI measured by two antennas on the same NIC. This CSI ratio is then projected onto a line that gives the largest breathing-to-noise ratio (BNR) plus variance on the complex plane. This process is repeated for all subcarriers, each of which has its own line for the CSI ratios to project onto. Peak detection is used to align the peaks along the projections, and PCA is applied with the first principal component retained. After this principal component is decomposed by VMD into intrinsic mode functions (IMFs), the IMF with the largest variation is selected as the respiratory waveform.

3 SYSTEM MODEL

This section describes the underlying assumptions and signal model used for extracting respiratory information from CSI data measured within a Wi-Fi system. The proposed WiRM algorithm is designed for use with orthogonal frequency-division multiplexing (OFDM), assuming that the subcarrier bandwidth is much less than the system coherence bandwidth and that the symbol time is much less than the system coherence time. These assumptions are well justified for indoor environments and the application of respiratory rate monitoring. Here, the relatively slow movements in the environments result in a large coherence time. Furthermore, the typical root-mean-square delay spread for an indoor environment is between 10 and 1,000 nanoseconds, resulting in a coherence bandwidth (in the megahertz range) much larger than the subcarrier bandwidths (in the kilohertz range) [35]. Under these assumptions, the channel can be considered time-invariant over the duration of a transmission symbol. Additionally, since the subcarrier bandwidth is much smaller than the coherence bandwidth,

each subcarrier can be modelled as experiencing frequency-flat fading.

WiRM requires a communication system with $A \geq 1$ transmit antennas on one NIC and $B \geq 2$ receive antennas on another NIC. The NIC provides an estimate of the time-dependent transfer function of the channel between the transmit and the receive antennas, i.e., the CSI. Assume that the CSI estimate provided by the NIC measured between a transmit antenna T_a (for $a \in \{1, 2, \dots, A\}$) and a receive antenna R_b (for $b \in \{1, 2, \dots, B\}$) is free of interference from the other transmitted signals, given a sufficient CSI estimation algorithm.

The CSI measured when the environment is static is defined as $H_{s,T_a,R_b}(f) \in \mathbb{C}$, where the subscript T_a, R_b indicates that the variable is measured from the transmit antenna T_a to the receive antenna R_b . Assuming only one multipath component interacts with a person breathing, we define $\alpha_{T_a,R_b}(f) \in \mathbb{R}^+$ to be the magnitude attenuation, λ the wavelength, D_{T_a,R_b} the distance the multipath travels when the breathing is paused, $\Delta d_{b,T_a,R_b}$ the depth of breathing, and θ_{T_a,R_b} the angle between the multipath and the vector tangent to the chest's motion during a breath. The CSI measured between the transmitter T_a and the receiver R_b is then defined as

$$H_{T_a,R_b}(t, f) = H_{s,T_a,R_b}(f) + \alpha_{T_a,R_b}(f) \exp\left(\frac{-j2\pi}{\lambda} \times (D_{T_a,R_b} + \Delta d_{b,T_a,R_b} \sin(\theta_{T_a,R_b})r(t))\right), \quad (1)$$

for each of the K subcarrier center frequencies, $f \in \{f_1, f_2, \dots, f_K\}$. The respiratory waveform $r(t) \in \mathbb{R}$ is periodic with an instantaneous frequency represented by $B_{\text{Hz}}(t) \in \mathbb{R}^+$ or $B(t) = 60B_{\text{Hz}}(t)$ (beats per minute). While the system model in (1) is adapted from TR-BREATH [12], we use a general periodic function $r(t)$ instead of assuming a sinusoidal respiratory waveform as in [12].

The system model in (1) is extended to include the effects of common noises in CSI measurements as follows:

$$\tilde{H}_{T_a,R_b}(t, f) = \kappa(t, f)H_{T_a,R_b}(t, f)e^{-j\eta(t,f)} + \epsilon(t, f), \quad (2)$$

where $\kappa(t, f) \in \mathbb{R}^+$ is log-normally distributed multiplicative noise, $\epsilon(t, f) \in \mathbb{C}$ is additive white Gaussian thermal noise, and $\eta(t, f) \in [-\pi, \pi]$ is uniformly distributed phase noise. With an abuse of notation, the system model will be referred to in discrete-time for the remainder of the paper as $\tilde{H}_{T_a,R_b}(n, f)$ for $n \in \{0, 1, \dots\}$, where $t = nT_s$ and T_s is the sampling period.

The task of respiration monitoring using CSI can be summarised as jointly estimating the respiratory waveform $r(n)$ and the instantaneous frequency of $r(n)$ (corresponding to the respiratory rate $B_{\text{Hz}}(n)$) from the noise-infected $\{\tilde{H}_{T_a,R_b}(n, f) : a \in \{1, \dots, A\}, b \in \{1, \dots, B\}\}$ as measured by the NIC.

3.1 Performance Criteria

The proposed algorithm will be compared against current state-of-the-art algorithms by using the average RMSE of the respiratory rate estimation $\tilde{B}_{\text{Hz}}(n)$ versus the ground truth $B_{\text{Hz}}(n)$. Additionally, we use the percentage of estimations within ± 3 BPM of the ground truth as a comparative metric

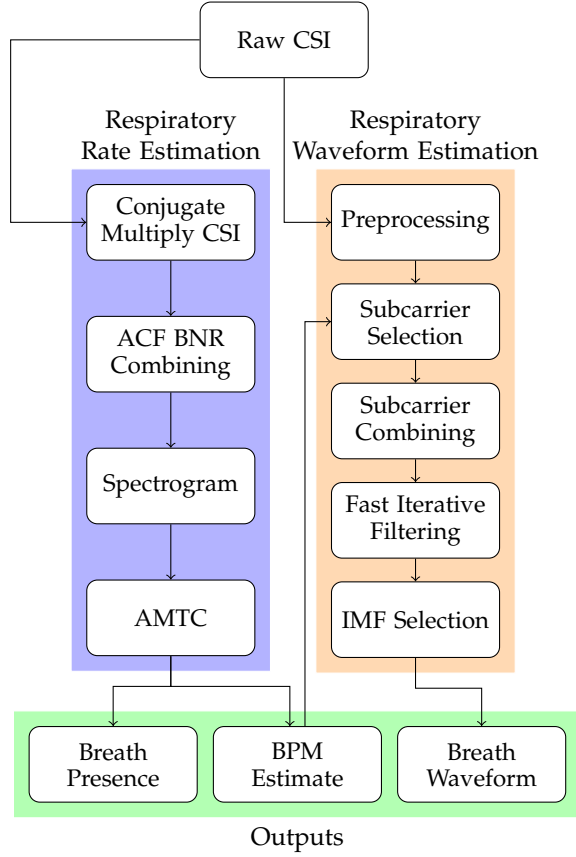


Fig. 1. Overview of the proposed WiRM algorithm.

to assess how consistently each method approximates the true respiratory rate.

To compare the respiratory waveform estimation, the absolute value of the correlation between the estimated waveform $\tilde{r}(n)$ and the ground truth $r(n)$ is computed. The absolute value is computed to account for if the algorithm has estimated the correct waveform, but it is negated as $\tilde{r}(n) = -r(n)$. The absolute correlation for a window of \tilde{N} time steps is computed via

$$|\rho_{r\tilde{r}}(n)| = \left| \frac{\sum_{i=n}^{n+\tilde{N}-1} (r(i) - \bar{r})(\tilde{r}(i) - \bar{\tilde{r}})}{\sqrt{\sum_{i=n}^{n+\tilde{N}-1} (r(i) - \bar{r})^2} \sqrt{\sum_{i=n}^{n+\tilde{N}-1} (\tilde{r}(i) - \bar{\tilde{r}})^2}} \right|, \quad (3)$$

where \bar{r} and $\bar{\tilde{r}}$ are the sample mean of $r(i)$ and $\tilde{r}(i)$ for $i \in \{n, n+1, \dots, n+\tilde{N}-1\}$, respectively. The correlation is computed over a sliding window, resulting in time-varying correlation values $|\rho_{r\tilde{r}}(n)|$ for $n \in \{0, 1, \dots\}$. The average and maximum of the absolute correlation values are used to compare the performance of each algorithm in estimating the respiratory waveform.

4 PROPOSED WIRELESS RESPIRATION MONITORING (WiRM) ALGORITHM

An overview of the proposed WiRM algorithm can be found in Figure 1 the respiratory rate estimation block produces an estimate of the current respiratory rate denoted $\tilde{B}_{Hz}(n)$, and a boolean indicator $\tilde{\Phi}(n)$ that shows whether or not a breath was detected within the CSI data for the current time

step. The respiratory-rate estimation procedure is described in Subsection 4.1. The output of the respiratory-waveform estimation block in Figure 1 is an estimate of the respiratory waveform denoted $\tilde{r}(n)$ as described in Subsection 4.2.

One novelty of the proposed algorithm lies in the use of the respiratory rate estimation to guide the respiratory waveform decomposition. This allows for an easier search over the set of decompositions and provides more confidence that the selected decomposed signal is indicative of breathing. While not a definitive method for ensuring the decomposed signal is a breath, this methodology greatly improves the decomposed signal's correlation with the ground truth. The entire estimation procedure is outlined in Figure 1.

4.1 Stage 1 – Respiratory Rate Estimation

The proposed respiratory rate estimation procedure can be found in Figure 1. Each block is summarised as follows.

- 1) The CSI data is preprocessed through conjugate multiplication. This nullifies phase noise within the CSI as shown in Figure 2 and detailed in Subsection 4.1.1.
- 2) The ACF of the magnitude and phase of the conjugate multiplied CSI is computed. These ACFs contain peaks that arise due to periodic signals embedded within the conjugate multiplied CSI. The ACFs are combined to accentuate the peaks corresponding to breath signals and minimise noise within the signal. More details are available in Subsection 4.1.2.
- 3) To observe which frequencies are present within the ACF, the Fourier transform is applied to obtain the power spectral density function. This process is repeated over a sliding window, where each power spectral density function forms a column of a spectrogram. Creating this spectrogram over sliding windows allows for the frequencies within the ACF to be observed as they change over time. More details are available in Subsection 4.1.3.
- 4) The adaptive multi-trace carving (AMTC) algorithm is finally applied to the spectrogram to achieve the final respiratory rate estimate. The AMTC algorithm uses transition probability functions from (13) which are proposed from observations on empirical respiratory data. These transition probability functions incorporate the dynamics of breathing into the AMTC algorithm while tracking the respiratory rate. More details are available in Subsection 4.1.4.

4.1.1 Conjugate Multiple CSI

Phase noise such as sampling clock offset, carrier frequency offset, jitter, and sampling time offset greatly impacts the reliability of CSI phase measurements. Fortunately, these sources of noise are all common to antennas attached to the same NIC and, equivalently, the same local oscillator. As such, we choose to cancel out the phase noise $\eta(t, f)$ from (2), by conjugate multiplication [25]. The conjugate multiplied CSI data exist on the arc of an ellipse in the complex plane, moving along the arc as the dynamic multipath changes [25], [36]. That is, the conjugate multiplied CSI moves along the arc as $r(t)$ changes in (1).

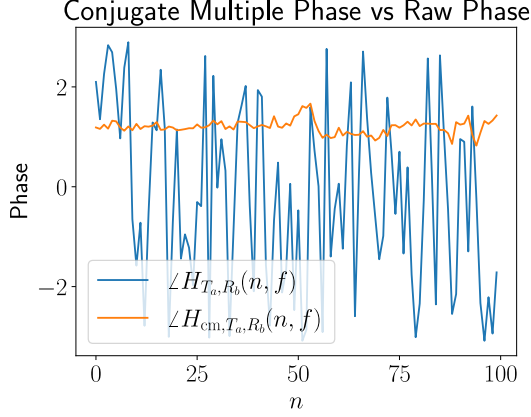


Fig. 2. The phase $\angle H_{T_a, R_b}(n, f)$ versus the conjugate multiplied phase $\angle H_{cm, T_a, R_b}(n, f)$. The figure shows improvements on the stability of the phase with the use of conjugate multiplication.

CSI data are collected in windows of length N , where N is chosen to ensure the respiratory waveform remains approximately stationary while still capturing at least one full breathing cycle. For each transmit antenna T_a for $a \in \{1, 2, \dots, A\}$ and receive antenna R_b for $b \in \{1, 2, \dots, B\}$, NK CSI values are collected, resulting in a total of $NKAB$ values. The conjugate multiplied CSI is computed by multiplying each CSI link with the complex conjugate of a reference link from the same transmitter to a fixed receiver R_1 , as defined in

$$H_{cm, T_a, R_b}(n, f) = H_{T_a, R_b}(n, f) \overline{H_{T_a, R_1}(n, f)}. \quad (4)$$

This operation is performed for $a \in \{1, 2, \dots, A\}$ and $b \in \{2, 3, \dots, B\}$, excluding the reference receiver R_1 , resulting in $L_{cm} = B(A - 1)$ conjugate multiplied links. For brevity, we denote each of these links as $H_{cm, i}$ where $i \in \{1, 2, \dots, L_{cm}\}$.

For every i -th conjugate multiplied link, the magnitude and the phase of the conjugate multiple CSI data are computed and represented by $|H_{cm, i}(n, f)|$ and $\angle H_{cm, i}(n, f)$ respectively.

4.1.2 ACF BNR Combining

The linear ACF is computed across time for each subcarrier and every conjugate multiple link for both the magnitude $|H_{cm, i}(n, f)|$ and phase $\angle H_{cm, i}(n, f)$. These ACFs are defined as

$$\begin{aligned} \mathbf{R}'_{|\cdot|, cm, i}(f) &= \begin{bmatrix} R_{|\cdot|, cm, i}(0, f) \\ R_{|\cdot|, cm, i}(1, f) \\ \vdots \\ R_{|\cdot|, cm, i}(N-1, f) \end{bmatrix} \\ \mathbf{R}'_{\angle, cm, i}(f) &= \begin{bmatrix} R_{\angle, cm, i}(0, f) \\ R_{\angle, cm, i}(1, f) \\ \vdots \\ R_{\angle, cm, i}(N-1, f) \end{bmatrix}, \end{aligned} \quad (5)$$

where $\mathbf{R}'_{|\cdot|, cm, i}(f)$ and $\mathbf{R}'_{\angle, cm, i}(f)$ are unit-less column vectors denoting the ACF of the magnitude and the ACF of the phase respectively for each subcarrier $f \in \{f_1, f_2, \dots, f_K\}$ and conjugate multiple link $i \in \{1, 2, \dots, L_{cm}\}$.

An important property of the ACF is that all white noise is correlated at a lag of zero; thus, the $\tau = 0$ sample is omitted from the ACFs $\mathbf{R}'_{|\cdot|, cm, i}(f)$ and $\mathbf{R}'_{\angle, cm, i}(f)$ [11]. This omission allows us to define

$$\begin{aligned} \mathbf{R}_{|\cdot|, cm, i}(f) &= \begin{bmatrix} R_{|\cdot|, cm, i}(1, f) \\ R_{|\cdot|, cm, i}(2, f) \\ \vdots \\ R_{|\cdot|, cm, i}(N-1, f) \end{bmatrix} \\ \mathbf{R}_{\angle, cm, i}(f) &= \begin{bmatrix} R_{\angle, cm, i}(1, f) \\ R_{\angle, cm, i}(2, f) \\ \vdots \\ R_{\angle, cm, i}(N-1, f) \end{bmatrix}, \end{aligned} \quad (6)$$

for each subcarrier $f \in \{f_1, f_2, \dots, f_K\}$ and conjugate multiple link $i \in \{1, 2, \dots, L_{cm}\}$. Two matrices for each conjugate multiple link are defined as

$$\begin{aligned} \mathbf{R}_{|\cdot|, cm, i} &= [\mathbf{R}_{|\cdot|, cm, i}(f_1), \mathbf{R}_{|\cdot|, cm, i}(f_2), \dots, \mathbf{R}_{|\cdot|, cm, i}(f_K)] \\ \mathbf{R}_{\angle, cm, i} &= [\mathbf{R}_{\angle, cm, i}(f_1), \mathbf{R}_{\angle, cm, i}(f_2), \dots, \mathbf{R}_{\angle, cm, i}(f_K)], \end{aligned} \quad (7)$$

where both $\mathbf{R}_{|\cdot|, cm, i}$ and $\mathbf{R}_{\angle, cm, i}$ are matrices with a dimension of $(N-1) \times K$ for each conjugate multiple link $i \in \{1, 2, \dots, L_{cm}\}$.

With $\mathbf{R}_{|\cdot|, cm, i}$ and $\mathbf{R}_{\angle, cm, i}$, an augmented ACF matrix $\mathbf{R}_{H_{cm, i}}$ of dimension $(N-1) \times 2K$ is defined as

$$\mathbf{R}_{cm, i} = [\mathbf{R}_{|\cdot|, cm, i}, \mathbf{R}_{\angle, cm, i}], \quad (8)$$

for $i \in \{1, 2, \dots, L_{cm}\}$.

All of the ACF matrices for each conjugate multiple link are then further augmented into one large matrix $\mathbf{R}_{H_{cm}}$ of dimension $(N-1) \times 2KL_{cm}$ defined as

$$\mathbf{R}_{cm} = [\mathbf{R}_{cm, 1}, \mathbf{R}_{cm, 2}, \dots, \mathbf{R}_{cm, L_{cm}}]. \quad (9)$$

The phase-invariance property of the ACF means that any periodic signals embedded within $|H_{cm, i}(n, f)|$ and $\angle H_{cm, i}(n, f)$ have periods that correspond to the peaks found within the ACF. Importantly, if there are common periodic signals in either $\mathbf{R}_{|\cdot|, cm, i}(f)$ or $\mathbf{R}_{\angle, cm, i}(f)$ for all subcarriers $f \in \{f_1, f_2, \dots, f_K\}$ and all conjugate multiple links $i \in \{1, 2, \dots, L_{cm}\}$, then the peaks corresponding to the common signal will align along the columns. With this property, the high dimensionality of \mathbf{R}_{cm} and noise within the ACFs, a strategy is needed to combine all of the ACFs (the columns of \mathbf{R}_{cm}). Such a strategy should accentuate the peaks in the ACFs caused by breath and minimise noise.

Breathing-to-noise-ratio (BNR) combining is used to combine signals that strengthens breath components while minimising frequency components outside of the range of normal breathing [26]. The BNR $\mathbb{B}(\mathbf{x})$ of a vector \mathbf{x} is described as

$$\mathbb{B}(\mathbf{x}) = \frac{\sum_{f \in \mathcal{B}} |\mathcal{F}(\mathbf{x})(f)|^2}{\sum_{f \in \mathcal{A}} |\mathcal{F}(\mathbf{x})(f)|^2}, \quad (10)$$

where $\mathcal{F}(\mathbf{x})$ is the FFT of \mathbf{x} , \mathcal{A} the set of all frequencies within the FFT of \mathbf{x} , and \mathcal{B} a subset of \mathcal{A} corresponding to the normal respiratory rate. That is,

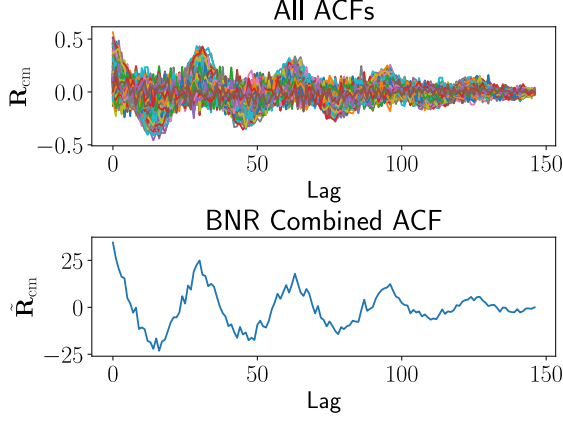


Fig. 3. All ACFs from \mathbf{R}_{cm} vs the BNR combined ACF $\tilde{\mathbf{R}}_{\text{cm}}$ with a breath signal present.

$\mathcal{B} = \{f \in \mathcal{A} | f_{b,\min} \leq f \leq f_{b,\max}\}$ where $f_{b,\min}$ and $f_{b,\max}$ correspond to the minimum and maximum normal respiratory rates, respectively [8].

Each column of \mathbf{R}_{cm} is weighted by its BNR, and the weighted columns are then summed to give the combined ACF column vector $\tilde{\mathbf{R}}_{\text{cm}}$ of length $(N-1)$, defined as

$$\tilde{\mathbf{R}}_{\text{cm}} = \sum_{j=0}^{2KL_{\text{cm}}} \mathbb{B}(\text{col}_j(\mathbf{R}_{\text{cm}})) \text{col}_j(\mathbf{R}_{\text{cm}}), \quad (11)$$

where $\text{col}_j(\mathbf{R}_{\text{cm}})$ is the j -th column of \mathbf{R}_{cm} for $j \in \{1, 2, \dots, 2KL_{\text{cm}}\}$. As evident in Figure 3, the BNR combining significantly accentuates the breathing signal embedded within \mathbf{R}_{cm} .

4.1.3 Spectrogram

By using the zoom FFT, the combined ACF $\tilde{\mathbf{R}}_{\text{cm}}$ is transformed into a power spectral density to produce a smoother frequency representation that only focuses on the frequency range of human breathing [37]. Note that the zoom FFT does not improve the frequency resolution, but rather creates a smoother frequency representation, similar to zero-padding.

A major disadvantage of using the power spectral density approach is due to the Heisenberg uncertainty principle [38]. The resolution in the frequency domain is limited based on the length of the signal recording, which with the stationarity constraint on N leads to poor frequency resolution. All frequencies within a given frequency difference $\Delta f = f_s/N$ (where f_s is the sampling frequency) are merged into one peak in the power spectral density plot, causing the poor frequency resolution. All frequencies within this frequency region or bin are sinc-interpolated, which, in practice, makes the maximum value of this peak represent an average of all of the frequencies within the bin. This fact allows the maximum value to still be useful as an approximate BPM estimate, which, when combined with the technique described in Subsection 4.2.2, resolves the frequency resolution issue.

To estimate both the breathing frequencies at the given time step n for the given window size N and how the frequencies change over time, a sliding window is employed with a total of W sliding windows. Here, two adjacent

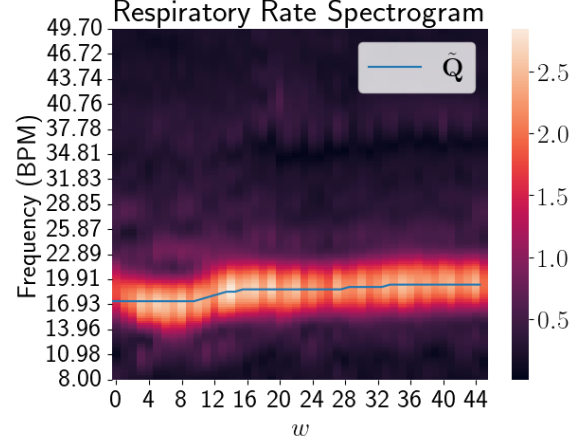


Fig. 4. The frequency spectrogram \mathbf{S} displays a respiratory trace $\tilde{\mathbf{Q}}$ from the AMTC algorithm over time. Note that the frequency resolution issue is apparent in this image, with the width in frequency of the respiratory trace being visibly large.

windows overlap by Y samples. Denote the start and end times of the w -th time window for $w \in \{0, 1, \dots, W-1\}$ as $w(N-Y)$ and $w(N-Y) + N-1$, respectively. The BNR-combined ACF (a length- $(N-1)$ column vector calculated according to (11)) for the w -th time window is then denoted as $\tilde{\mathbf{R}}_{\text{cm},w}$.

A spectrogram \mathbf{S} of dimension $(N-1) \times W$ is created by using the sliding-window BNR-combined ACF $\tilde{\mathbf{R}}_{\text{cm},w}$ for $w \in \{0, 1, \dots, W-1\}$ as follows:

$$\mathbf{S} = [\mathcal{F}_z(\tilde{\mathbf{R}}_{\text{cm},0}), \mathcal{F}_z(\tilde{\mathbf{R}}_{\text{cm},1}), \dots, \mathcal{F}_z(\tilde{\mathbf{R}}_{\text{cm},W-1})], \quad (12)$$

where the magnitude of the zoom FFT of a vector \mathbf{x} is denoted as $\mathcal{F}_z(\mathbf{x})$. The output of the zoom FFT is a column vector of length $N-1$ representing $N-1$ evenly spaced frequencies from $f_{b,\min}$ to $f_{b,\max}$. This results in the spectrogram \mathbf{S} being a matrix of dimension $(N-1) \times W$ with $N-1$ frequencies and W time steps. Figure 4 shows an example of a real breath signal as it evolves over time within the spectrogram \mathbf{S} .

This procedure is very similar to the power spectral density generation facilitated by the short-time Fourier transform [39]. However, a major difference between the short-time Fourier transform and the approach outlined in (12) is that the power spectral density for each time window is computed from a combination of subcarriers, which could change from one window to the next as described in (11).

4.1.4 AMTC

The AMTC algorithm estimates a trace \mathbf{Q} that describes how a frequency changes over time within a spectrogram [40]. Here, we choose this algorithm for its efficient computation and its ability to embed transition probabilities into the estimation of frequency traces. AMTC assumes that frequency transitions from $Q(n-1)$ to the next frequency $Q(n)$ follows a Markov process. The exact probability distribution that describes the likelihood of the frequency transition is

system-dependent as:

$$\log(P_{\mathbf{Q}}(\mathbf{q})) = \log(P_{Q(0)}(q_0)) + \sum_{w=1}^{W-1} \log(P_{Q(w)|Q(w-1)}(q_w|q_{w-1})), \quad (13)$$

where $\mathbf{q} = [q_0, q_1, \dots, q_{W-1}]$, $P_{Q(0)}(q_0)$ is the probability of the first frequency $Q(0)$ occurring, and $P_{Q(w)|Q(w-1)}(q_w|q_{w-1})$ the conditional probability of the frequency $Q(w)$ occurring given that the previous frequency is $Q(w-1)$ for $Q(w) \in \{f_1, f_2, \dots, f_K\}$ and $w \in \{0, 1, \dots, W-1\}$.

Using AMTC, we aim to jointly estimate the respiratory rates $Q(w) \in \{f_1, f_2, \dots, f_{N-1}\}$ for all sliding time windows $w \in \{0, 1, \dots, W-1\}$ from the spectrogram \mathbf{S} . Define the estimated respiratory rate trace as $\tilde{\mathbf{Q}} = [\tilde{Q}(0), \tilde{Q}(1), \dots, \tilde{Q}(W-1)]$. For the purposes of respiratory rate tracking, we assume $P_{Q(1)}(q_1)$ and $P_{Q(w)|Q(w-1)}(q_w|q_{w-1})$ from (13) as a uniform distribution and a zero-mean Gaussian distribution, respectively as:

$$P_{Q(0)}(q_1) = \frac{1}{N-1},$$

$$P_{Q(w)|Q(w-1)}(q_w|q_{w-1}) = \frac{1}{\sigma\sqrt{2\pi}} e^{-\frac{(q_w - q_{w-1})^2}{2\sigma^2}}, \quad (14)$$

for all $w \in \{0, 1, \dots, W-1\}$ where σ is the standard deviation of the Gaussian distribution.

The choice of a uniform distribution is justified by the lack of prior knowledge of what the respiratory rate may be at $w = 0$ and, as such, all frequencies $Q(0) \in \{f_1, f_2, \dots, f_{N-1}\}$ are assumed equally likely. The zero-mean Gaussian distribution is proposed based on evidence found during the analysis of a respiratory waveform dataset [41]. Curve fitting is applied to the dataset to obtain $\sigma = 4.552$.

The AMTC algorithm produces a frequency trace of length W by finding the trace that maximises the energy along the trace from \mathbf{S} , rewarded by the frequency transition probability. This allows the trace to follow the path of maximal energy while also maintaining probable frequency transitions. The estimated frequency trace is calculated as

$$\tilde{\mathbf{Q}} \in \underset{\mathbf{q}}{\operatorname{argmax}} \left(E(\tilde{\mathbf{q}}) + \Lambda \log(P_{\mathbf{Q}}(\tilde{\mathbf{q}})) \right), \quad (15)$$

where $E(\tilde{\mathbf{q}})$ is the total energy of the trace taken from \mathbf{S} , $\Lambda \in \mathbb{R}^+$ a tuneable smoothing parameter, and $\tilde{\mathbf{q}} \in \{f_1, f_2, \dots, f_{N-1}\}^{N-1}$. Here, ties in $\tilde{\mathbf{Q}}$ are broken arbitrarily.

The respiratory rate estimation for the current timestep $\tilde{B}_{\text{Hz}}(n)$ is finally computed as

$$\tilde{B}_{\text{Hz}}(n) = \tilde{Q} \left(\left\lceil \frac{n - N + 1}{N - Y} \right\rceil \right), \quad (16)$$

for $n \in \{0, 1, \dots, W(N - Y) + N - 1\}$ and where $\lceil x \rceil = \max(0, \lceil x \rceil)$.

Along with the frequency trace $\tilde{\mathbf{Q}}$, the AMTC algorithm also returns the trace $\Phi = [\Phi(0), \Phi(1), \dots, \Phi(W-1)]$, where $\Phi(w)$ equals 1 if breath is detected in the w -th window and 0 otherwise [40]. Breathing detection for each time step is computed similarly to (16).

4.1.5 Summary

Algorithm 1 summarises the proposed respiratory rate estimation algorithm, where $\text{AMTC}(\mathbf{S})$ denotes performing the AMTC algorithm on the spectrogram \mathbf{S} , and $\text{col}_w(\mathbf{S})$ denotes the w -th column of \mathbf{S} .

Algorithm 1: WiRM Stage 1 – Respiratory Rate Estimation

Input : W time windows of N samples of CSI data $H_{T_a, R_b}(n, f)$ for T_a , $a \in \{1, 2, \dots, A\}$ and R_b , $b \in \{1, 2, \dots, B\}$

Output: The current BPM estimate $\tilde{B}_{\text{Hz}}(n)$ and the boolean indicator of breath presence $\tilde{\Phi}(n)$

$\mathbf{S} \leftarrow$ empty 2D matrix of dimension $(N-1) \times W$;

for $w \in \{1, 2, \dots, W\}$ **do**

compute $H_{\text{cm}, i}(n, f)$ for $i \in \{1, 2, \dots, L_{\text{cm}}\}$ via (4);

compute $\mathbf{R}_{|\cdot|, \text{cm}, i}(f)$ and $\mathbf{R}_{\angle, \text{cm}, i}(f)$ via (6);

compute \mathbf{R}_{cm} via (8) and (9);

compute $\tilde{\mathbf{R}}_{\text{cm}}$ via (11);

$\text{col}_w(\mathbf{S}) \leftarrow \tilde{\mathbf{R}}_{\text{cm}}$;

end

$\tilde{\mathbf{Q}}, \Phi \leftarrow \text{AMTC}(\mathbf{S})$;

$\tilde{B}_{\text{Hz}}(n) \leftarrow \tilde{Q}(\left\lceil \frac{n - N + 1}{N - Y} \right\rceil)$;

$\tilde{\Phi}(n) \leftarrow \Phi(\left\lceil \frac{n - N + 1}{N - Y} \right\rceil)$;

return $\tilde{B}_{\text{Hz}}(n), \tilde{\Phi}(n)$

4.2 Stage 2 – Respiratory Waveform Estimation

The proposed respiratory waveform estimation procedure can be found in Figure 1. Each block is summarised as follows.

- 1) The raw CSI data is pre-processed similarly to Subsection 4.1.1; however, a much longer time period is measured, where the non-stationary dynamics of breathing can be observed. This is detailed in Subsection 4.2.1.
- 2) The subcarrier that most strongly contains the respiratory rate estimation from Subsection 4.1.4 is selected as the primary subcarrier, as detailed further in Subsection 4.2.2.
- 3) The primary subcarrier may still contain noise and so a combining procedure is proposed. More details are available in Subsection 4.2.3.
- 4) The fast iterative filtering algorithm is employed to decompose the combined subcarrier into a set of IMFs, one of which is the estimated respiratory waveform. More details are available in Subsection 4.2.4.
- 5) The respiratory waveform is selected from the set of IMFs as further detailed in Subsection 4.2.5, giving the final estimated respiratory waveform $\tilde{r}(n)$.

4.2.1 Pre-Processing

As previously noted in Subsection 4.1.3, the frequency resolution of the FFT is directly determined by the duration of the observed signal. Specifically, shorter observation windows result in poorer frequency resolution, while longer

windows yield better frequency resolution. However, in the context of respiration monitoring, longer observation periods increase the likelihood of changes in the respiratory rate, resulting in non-stationary behaviour. Fortunately, iterative filtering allows for the separation of such non-stationary signals [42].

To improve the ability of iterative filtering to distinguish signals of similar frequency from each other (i.e., improve the frequency resolution), a window of \tilde{N} CSI samples are collected where $\tilde{N} > N$ [43]. Recall that N was chosen such that the respiratory rate could be considered stationary, so this constraint does not exist on \tilde{N} . The \tilde{N} samples of raw CSI data is conjugate multiplied in (4) to produce $H_{\text{cm},i}(n, f)$ for conjugate multiple link $i \in \{1, 2, \dots, L_{\text{cm}}\}$, time $n \in \{0, 1, \dots, \tilde{N} - 1\}$, and frequency $f \in \{f_1, f_2, \dots, f_K\}$.

The magnitude and phase of the conjugate multiplied CSI data are computed and z -score normalised to make them unitless signals so that we can combine them for noise removal in Subsection 4.2.3. The z -score normalisation was not previously required in Subsection 4.1 since the ACF already eliminates the units of the signal. The z -score normalisation of a vector \mathbf{x} is defined as

$$z(\mathbf{x}) = \frac{\mathbf{x} - \mu_{\mathbf{x}}}{\sigma_{\mathbf{x}}}, \quad (17)$$

where $\mu_{\mathbf{x}}$ is the mean of \mathbf{x} , and $\sigma_{\mathbf{x}}$ is the standard deviation. The subtraction $\mathbf{x} - \mu_{\mathbf{x}}$ denotes the element-wise subtraction of the scalar mean from each element of the vector \mathbf{x} .

The $\tilde{N} \times K$ dimension augmented matrices $\mathbf{Z}_{|\cdot|, \text{cm}, i}$ and $\mathbf{Z}_{\angle, \text{cm}, i}$ are defined as

$$\begin{aligned} \mathbf{Z}_{|\cdot|, \text{cm}, i} &= \begin{bmatrix} z(|H_{\text{cm},i}(n, f_1)|), z(|H_{\text{cm},i}(n, f_2)|), \dots, \\ z(|H_{\text{cm},i}(n, f_K)|) \end{bmatrix} \\ \mathbf{Z}_{\angle, \text{cm}, i} &= \begin{bmatrix} z(\angle H_{\text{cm},i}(n, f_1)), z(\angle H_{\text{cm},i}(n, f_2)), \dots, \\ z(\angle H_{\text{cm},i}(n, f_K)) \end{bmatrix} \end{aligned} \quad (18)$$

for conjugate multiple link $i \in \{1, 2, \dots, L_{\text{cm}}\}$ and time $n \in \{0, 1, \dots, \tilde{N} - 1\}$. These matrices are then further augmented into one large matrix as

$$\begin{aligned} \mathbf{Z}_{\text{cm}} &= \begin{bmatrix} \mathbf{Z}_{|\cdot|, \text{cm}, 1}, \mathbf{Z}_{\angle, \text{cm}, 1}, \mathbf{Z}_{|\cdot|, \text{cm}, 2}, \mathbf{Z}_{\angle, \text{cm}, 2}, \dots, \\ \mathbf{Z}_{|\cdot|, \text{cm}, L_{\text{cm}}}, \mathbf{Z}_{\angle, \text{cm}, L_{\text{cm}}} \end{bmatrix} \end{aligned} \quad (19)$$

which forms the $\tilde{N} \times 2KL_{\text{cm}}$ matrix \mathbf{Z}_{cm} .

4.2.2 Subcarrier Selection

The subcarrier selection procedure is performed using the respiratory estimate from Subsection 4.1.4. As new length- N time windows are processed, a sliding AMTC is performed to compute a respiratory estimate for the last time window. The respiratory estimate for this last time window is used in the subcarrier selection procedure.

We propose that the subcarrier magnitude or phase (i.e., the columns of \mathbf{Z}_{cm}) that contains a strong frequency component at the respiratory rate \tilde{B}_{Hz} within the last N samples is chosen as the primary subcarrier. If we denote the element within \mathbf{Z}_{cm} at the i -th row and the j -th column

as $(\mathbf{Z}_{\text{cm}})_{i,j}$, then the discrete-time Fourier transform of each column of \mathbf{Z}_{cm} evaluated at the breathing frequency \tilde{B}_{Hz} is computed as

$$\begin{bmatrix} F_1 \\ F_2 \\ \vdots \\ F_{2KL_{\text{cm}}} \end{bmatrix}^T = \begin{bmatrix} \sum_{n=\tilde{N}-1-N}^{\tilde{N}-1} (\mathbf{Z}_{\text{cm}})_{n,1} e^{-j2\pi \tilde{B}_{\text{Hz}} n T_s} \\ \sum_{n=\tilde{N}-1-N}^{\tilde{N}-1} (\mathbf{Z}_{\text{cm}})_{n,2} e^{-j2\pi \tilde{B}_{\text{Hz}} n T_s} \\ \vdots \\ \sum_{n=\tilde{N}-1-N}^{\tilde{N}-1} (\mathbf{Z}_{\text{cm}})_{n,2KL_{\text{cm}}} e^{-j2\pi \tilde{B}_{\text{Hz}} n T_s} \end{bmatrix}^T, \quad (20)$$

where $[F_1, F_2, \dots, F_{2KL_{\text{cm}}}]$ is a row vector denoting the discrete-time Fourier transform evaluated at a frequency of \tilde{B}_{Hz} for the last N elements of each column of \mathbf{Z}_{cm} , and T_s is the sample period.

The index of the primary subcarrier c_{ps} is determined as

$$c_{\text{ps}} \in \underset{c}{\text{argmax}} (|F_c|) \quad (21)$$

for $c \in \{1, 2, \dots, 2KL_{\text{cm}}\}$. Ties in c_{ps} are broken by selecting the first index that gives the maximum magnitude $|F_c|$, yielding a single value c_{ps} . We can extract the magnitude and phase of the primary subcarrier as $|F_{c_{\text{ps}}}|$ and $\angle F_{c_{\text{ps}}}$, respectively.

This entire process is equivalent to taking the magnitude of the discrete-time Fourier transform of the last N samples of each subcarrier's magnitude and phase, evaluated at the frequency of breathing and choosing the largest magnitude as the primary subcarrier.

4.2.3 Subcarrier Combining

Even though the primary subcarrier contains a strong frequency component at the respiratory rate \tilde{B}_{Hz} , there may still be significant noise present. As such, we now present a combining strategy that is a variant of the breathing-to-noise ratio combining strategy presented in Subsection 4.1.2. From (1), it can be seen that the breathing signal must be in phase or 180° out of phase across subcarriers. An appropriate phase shift (either 0° or 180°) can be chosen and applied to each subcarrier to align it with the primary subcarrier. The phase shift can be achieved by either negating the subcarrier or not. Whether or not a subcarrier must be negated can be determined through (20) and (21) as

$$\beta_c = \begin{cases} 1, & |\angle F_{c_{\text{ps}}} - \angle F_c| \leq \frac{\pi}{2} \\ -1, & \text{otherwise} \end{cases}, \quad (22)$$

for $c \in \{1, 2, \dots, 2KL_{\text{cm}}\}$. The insight here is that if a given subcarrier contains the frequency of breathing approximately in phase with the primary subcarrier, then the absolute difference between the phase at the breath frequency \tilde{B}_{Hz} should at least be less than $\pi/2$.

Additionally, each subcarrier during the combining process can be scaled by their relative magnitudes to the primary subcarrier. Doing so ensures that subcarriers that contain a strong frequency component at \tilde{B}_{Hz} are given higher weights than subcarriers that do not. The overall combining procedure combines the columns of \mathbf{Z}_{cm} into a combined subcarrier column vector $\tilde{\mathbf{p}}$ of length \tilde{N} as

$$\tilde{\mathbf{p}} = \sum_{c=1}^{2KL_{\text{cm}}} \beta_c \frac{|F_c|}{|F_{c_{\text{ps}}}|} \text{col}_c(\mathbf{Z}_{\text{cm}}), \quad (23)$$

where $\text{col}_c(\mathbf{Z}_{\text{cm}})$ denotes the c -th column of \mathbf{Z}_{cm} .

4.2.4 Fast Iterative Filtering

The combined subcarrier $\tilde{\mathbf{p}}$ contains a strong component at the respiratory rate frequency. Unfortunately, it may also still contain noise such as that from non-respiration motion or environment. To produce an estimate of the respiratory waveform, the combined subcarrier can be decomposed into a set of IMFs where, if the decomposition was successful, one of the IMFs is the estimated respiratory waveform. Given the frequency resolution constraints and the non-stationary dynamics of respiration as described in Subsection 4.2.1, the fast iterative filtering (FIF) algorithm is chosen to perform the decomposition [42], [44]. FIF algorithm has proven convergence, efficiency, and ability to decompose similar non-stationary frequencies [43].

The FIF algorithm decomposes a vector $\tilde{\mathbf{p}}$ into a matrix with dimension $\tilde{N} \times D$, where D is the number of IMFs generated by the FIF algorithm. D depends on the oscillatory modes of $\tilde{\mathbf{p}}$ and is varying. The application of FIF to $\tilde{\mathbf{p}}$ is expressed as

$$\text{FIF}(\tilde{\mathbf{p}}) = [\text{IMF}_1, \text{IMF}_2, \dots, \text{IMF}_D], \quad (24)$$

where IMF_i is a length- \tilde{N} column vector denoting the i -th IMF for $i \in \{0, 1, \dots, \tilde{D}\}$.

FIF can potentially suffer from mode-splitting, i.e., oscillatory modes from one physical phenomenon spread across multiple IMFs [45]. It produces a filter width of

$$l = 2 \left\lfloor \chi \frac{m}{k} \right\rfloor, \quad (25)$$

where m is the number of points in the signal, k the number of extrema points in the signal, and χ a tuning parameter. The value of χ must be tuned to avoid mode-splitting and is chosen according to Section 5.

4.2.5 IMF Selection

The respiratory waveform must now be selected from the matrix of IMFs $\text{FIF}(\tilde{\mathbf{p}})$. To this end, we employ a similar technique to Subsection 4.2.2. Given that we have a respiratory rate estimate \tilde{B}_{Hz} , which is the respiratory rate that is computed from the previous N time steps, we propose that the IMF with its dominant frequency component closest to \tilde{B}_{Hz} is selected as the respiratory waveform.

If we define a column vector containing the last N elements of IMF_i as $\tilde{\text{IMF}}_i$ for $i \in \{1, 2, \dots, D\}$, then the dominant frequency component is computed as

$$f_{\text{peak},i} \in \underset{f}{\text{argmax}} \left(\left| \text{row}_f(|\mathcal{F}_z(\tilde{\text{IMF}}_i)|) \right| \right) \quad (26)$$

for $i \in \{1, 2, \dots, D\}$. Here, $\text{row}_i(\mathbf{x})$ denotes the i -th row of a column vector \mathbf{x} , and $f_{\text{peak},i} \in [f_{\text{b,min}}, f_{\text{b,max}}]$ is the dominant frequency component with ties within argmax_f being broken by choosing the first value.

The index i_b of the IMF that has its peak closest to the respiratory waveform frequency \tilde{B}_{Hz} is computed as

$$i_b \in \underset{i}{\text{argmin}} \left(\left| f_{\text{peak},i} - \tilde{B}_{\text{Hz}} \right| \right) \quad (27)$$

for $i \in \{1, 2, \dots, D\}$. Here, ties in i_b are broken arbitrarily yielding a single value i_b .

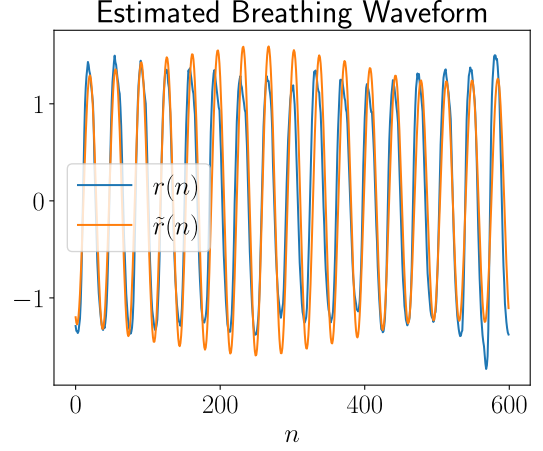


Fig. 5. The estimated breath waveform $\tilde{r}(n)$ compared to the actual respiratory waveform $r(n)$ measured during a polysomnography test.

Finally, the respiratory waveform is estimated as

$$\tilde{\mathbf{r}} = \text{col}_{i_b}(\text{FIF}(\tilde{\mathbf{p}})). \quad (28)$$

This selected IMF is the final estimated respiratory waveform representing the motion of the chest as a person breathes, as shown in Figure 5. This final waveform of length \tilde{N} is a non-stationary signal that appropriately captures the dynamics of a person's breath allowing for its use in medical scenarios.

Algorithm 2 summarises the respiratory waveform estimation algorithm.

Algorithm 2: WiRM Stage 2 – Respiratory Waveform Estimation

Input : $L_{\text{cm}}K\tilde{N}$ CSI measurements $H(n, f)$, and the current respiratory rate estimate in Hertz $\tilde{B}_{\text{Hz}}(n)$.

Output: The respiratory waveform estimate $\tilde{r}(n)$.

for link $i \in \{1, 2, \dots, L_{\text{cm}}\}$ **do**

 | compute $\mathbf{Z}_{|\cdot|, \text{cm}, i}$ and $\mathbf{Z}_{\angle, \text{cm}, i}$ as in (18);

end

form \mathbf{Z}_{cm} as in (19);

compute $[F_1, F_2, \dots, F_{2KL_{\text{cm}}}]$ as in (20);

find the primary subcarrier index c_{ps} as in (21);

compute the combined subcarrier $\tilde{\mathbf{p}}$ as in (23);

compute $\text{FIF}(\tilde{\mathbf{p}})$ as in (24);

find the frequency peaks of each IMF, $f_{\text{peak},i}$ for $i \in \{1, 2, \dots, D\}$, as in (26);

find the IMF index i_b with the closest frequency peak to $\tilde{B}_{\text{Hz}}(n)$ as in (27);

$\tilde{\mathbf{r}} \leftarrow \text{col}_{i_b}(\text{FIF}(\tilde{\mathbf{p}}))$;

return $\tilde{\mathbf{r}}$

5 PERFORMANCE EVALUATION

The performance of the proposed algorithm WiRM is evaluated and compared against three state-of-the-art methods, namely, Position-Free Breath (referred to as Pos-Free Breath) [13], TR-BREATH [12], and SMARS [11]. The three criteria

TABLE 1
Common Parameter Settings

Parameter Name	Value
Number of subcarriers (K)	114
Sample frequency (f_s)	9.9Hz
Number of transmit antennas (A)	2
Number of receive antennas (B)	2
Number of breaths	1

for comparison are (i) the RMS error of the estimated respiratory rate $\tilde{B}(n)$ compared to the ground truth, (ii) the percentage of estimated $\tilde{B}(n)$ within 3 BPM of the ground truth, and (iii) the absolute correlation of the estimated waveform $\tilde{r}(n)$ compared to the ground truth. Comparisons are performed exclusively at the time steps n , where each method yields a respiratory rate and/or waveform estimate. Of these state-of-the-art methods, only Pos-Free Breath computes a respiratory waveform. As such, only Pos-Free Breath and WiRM are compared for respiratory waveform estimation. The absolute value of the correlation is used because both Pos-Free Breath and WiRM could potentially produce an inverted respiratory waveform compared to the ground truth, resulting in a high magnitude but negative correlation.

In general, the results using existing methods are less favourable compared to those reported in the literature because the latter is based on an indicator if breath has been detected or not. The accuracy of existing methods has previously been evaluated at time steps where the method has detected that a breath is present. However, to maintain fairness to all methods (given that the datasets used *always* contain breathing), we evaluate the accuracy for all time-steps, not just those where a breath is detected.

5.1 Parameter Settings

The parameters specific to our proposed algorithm are configured as follows. The amount of samples collected for respiratory rate estimation $N = 150$, the number of windows $W = 46$, the overlap of each window $Y = 140$ (i.e., approximately 1 second between respiration rate estimates), the AMTC smoothing parameter $\Lambda = 0.5$, the number of samples collected for respiratory waveform estimation $\tilde{N} = 600$, and the fast iterative filtering tuning parameter $\chi = 2.7$. The maximum and minimum respiratory rates are defined as $[f_{b,\min}, f_{b,\max}] = [0.133\text{Hz}, 0.833\text{Hz}]$, which corresponds to approximately 8BPM and 50BPM respectively.

The parameters that are common amongst all methods are derived from the open-source dataset outlined in Subsection 5.2.1. These common parameters are listed in Table 1.

5.2 Respiratory Rate Performance

5.2.1 Dataset

The public and open-source radio frequency polysomnography dataset [46] is used to evaluate the performance of each method. It was created for contactless respiration monitoring using radio frequency measurements. The dataset consists of 20 individuals having a polysomnography examination, while the CSI and other radio frequency parameters are recorded simultaneously.

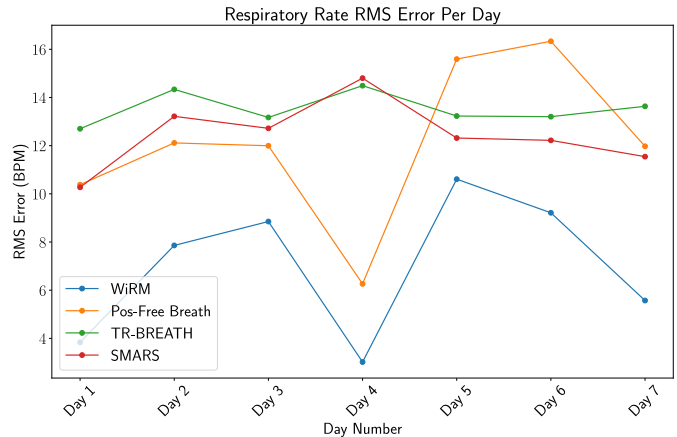


Fig. 6. The RMS error measured in BPM of the estimated respiratory rate $\tilde{B}(n)$ versus the ground truth data $B(n)$ for seven nights worth of radio frequency polysomnography data.

The polysomnography data consist of measurements from a chest rip, abdomen rip, thermocouple, and nasal cannula. The ground truth respiratory waveform is the direct chest rip measurement, whereas the respiration rate is derived from the polysomnography measurements using a combination of low-pass filtering and the zero-crossing method.

The CSI data consist of complex numbers representing the gain and phase shift of the channel at the current time step and subcarrier, as measured by the NIC. These data are used directly as the input to each respiration monitoring algorithm with no pre-processing.

5.2.2 Results

The RMS error of each method for each of the seven nights of radio frequency polysomnography data is shown in Figure 6. It can be seen that WiRM outperforms all other methods, regularly achieving a lower RMS error per night. When compared against the best-performing state-of-the-art method, WiRM achieves an overall average RMS error improvement of 38%.

Another useful performance metric is the percentage of estimations within a given absolute error of the ground truth. An example of this metric for each method is presented in Figure 7. As shown, for the provided night, WiRM has over 50% of its samples within 1 BPM of the ground truth respiratory rate and over 30% within the error range of $[1, 3]$ BPM. These results demonstrate that WiRM computes a respiratory rate estimate that closely follows the ground truth for the majority of estimates on the shown night.

This ability for WiRM to track the respiratory rate over time is further displayed in Figure 8, where the estimated respiratory rate $\tilde{B}(n)$ is closely following the ground truth $B(n)$. Figure 8 also contains red shading where the method was unable to detect the presence of breathing. Notably, WiRM correctly identifies the presence of a breath within the CSI data for 92.2% of the time for the given night.

Performing a similar analysis across all days, measuring the percentage of samples within 3 BPM of the ground truth respiratory rate $B(n)$ yields Figure 9. For most of the nights within the radio-frequency polysomnography

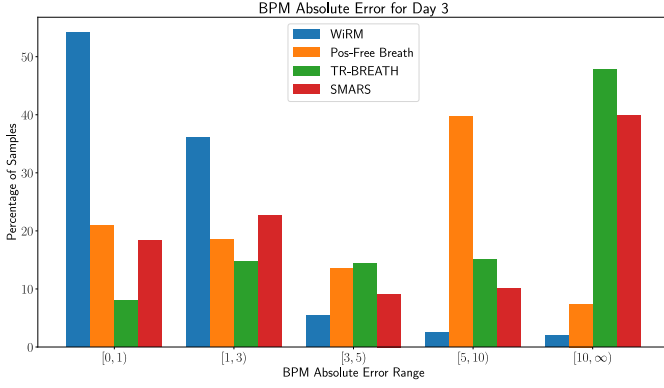


Fig. 7. Percentage of samples where each method achieves an absolute error within specified ranges for one night of data. The vertical axis shows the proportion of samples relative to the total sample count.

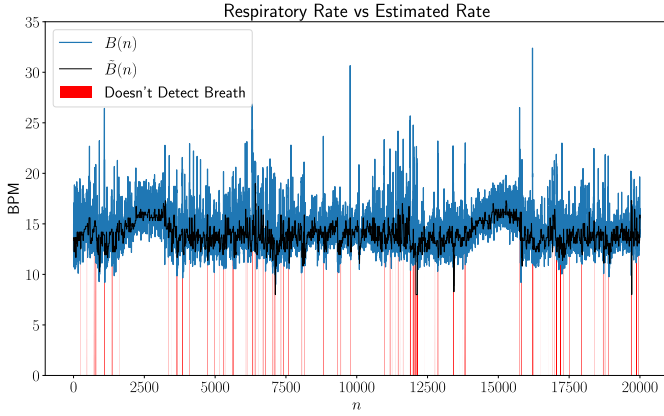


Fig. 8. An example of WiRM tracking the ground truth respiratory rate $B(n)$ over one night's worth of data from the radio frequency polysomnography dataset.

dataset, WiRM is observed to have a higher percentage of samples within 3 BPM of absolute value error. Although not outperforming the current state-of-the-art for all of the nights against this metric, it still achieves an average improvement of 33.1% across all nights over the best performing method for any given night.

5.3 Respiratory Waveform Performance

5.3.1 Dataset

The performance evaluation of the respiratory waveform is conducted using the same open-source dataset described in Subsection 5.2.1.

5.3.2 Results

Here we compare the average absolute correlation $|\rho|$ of the produced waveform $\tilde{r}(n)$ with the ground truth waveform $r(n)$ obtained from the chest rip of the radio frequency polysomnography dataset. Defined as the average of $|\rho_{r\tilde{r}}(n)|$, the values of $|\rho|$ are shown in Figure 10 where the maximum achieved correlation per night is also displayed. It is evident from the figure that WiRM improves the average and maximum correlation by 178.3% and 55.4%, respectively, compared to the state-of-the-art approach.

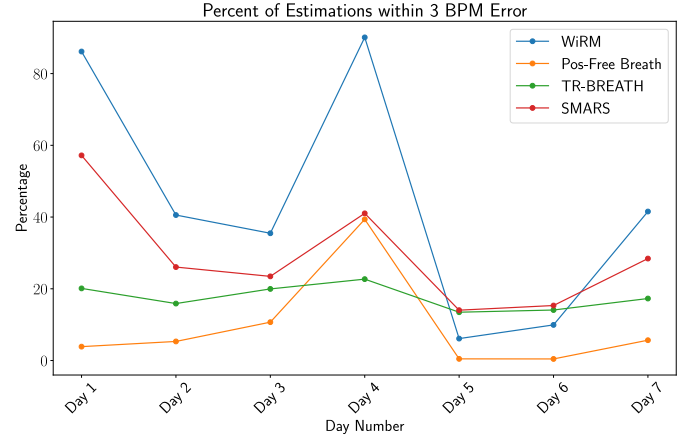


Fig. 9. The percentage of time that each method is within an absolute error of 3 BPM compared to the ground truth of $B(n)$.

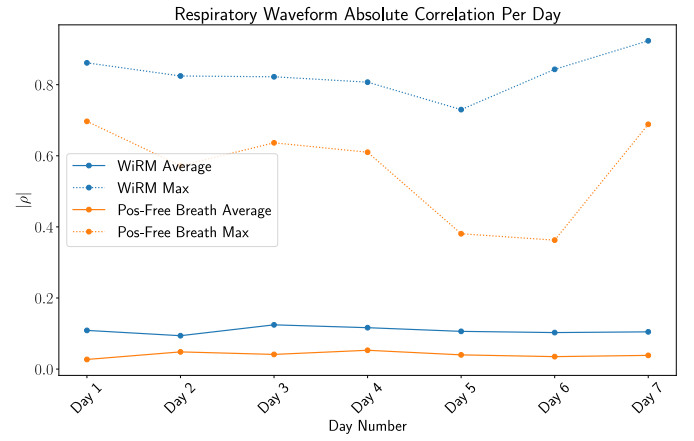


Fig. 10. The average and maximum absolute value of the correlation per night of WiRM compared to Pos-Free Breath.

5.4 Robustness Against Noise

5.4.1 Simulation Toolkit and Simulated Dataset

In this paper, we develop a simulation toolkit for fast and consistent comparison of wireless respiration-monitoring methods under various forms of noise. Based on (2), it allows configurable control over noise, static and dynamic components, including the breath waveform and the number of breaths. All stochastic elements are seeded for reproducibility. Simulation configurations are stored with results to ensure consistent conditions across different estimation algorithms.

The simulated data are idealistic in their construction, allowing for scenarios where the error of some of the estimation methods is zero. This is neither indicative of the performance in the real world nor the purpose of the simulation. Rather, the simulation allows for the behaviour of different respiration monitoring solutions to be compared when subjected to three kinds of noise: thermal (additive), multiplicative, and phase. Since the ability to vary noise precisely and measure its impact is not currently available in the literature, it proves valuable in evaluating the robustness of respiration monitoring methods.

Each type of noise is generated as described in Subsec-

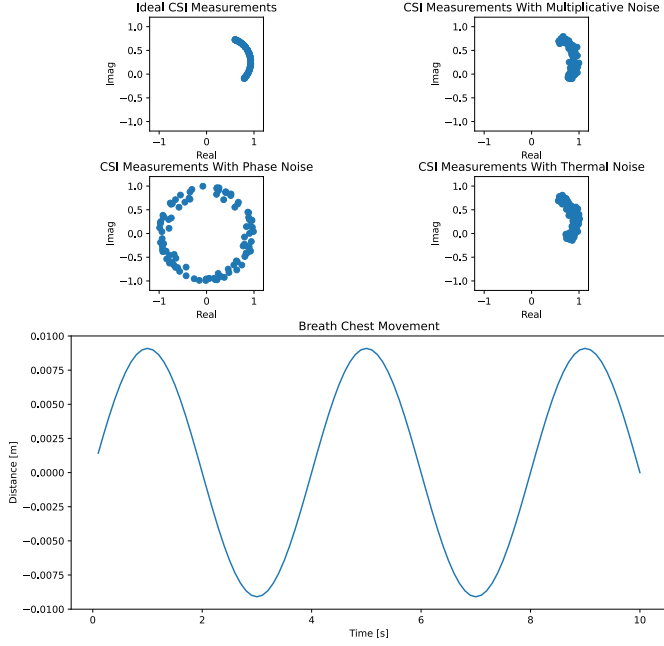


Fig. 11. The output of the simulated CSI and breathing values using the simulation toolkit for one breather.

tion 3. The noise levels can be varied by performing simulations where the only changing parameter is the standard deviation of the noise or in the case of phase noise, whether it is present or not. An example of the simulated CSI and respiration data is found in Figure 11.

The parameters for all simulations described in Section 5.4.2 are chosen to align with the public open source dataset as shown in Table 1. An ideal sinusoidal respiratory waveform is chosen as $r(n)$. We select the remaining simulation parameters as shown in Table 2.

To produce the results in Subsection 5.4.2, each of the simulations is run three times, each with a new seed, which in turn produces a new simulated environmental condition. For each of these runs, the RMS error of the respiratory rate and absolute correlation of the respiratory waveform are computed. The overall result is the average of all three runs. This process is repeated for varying levels of thermal, multiplicative, and phase noise.

5.4.2 Results

Using the simulated dataset, the average respiratory rate RMS errors are shown in Tables 3, 4, and 5, whereas the average absolute correlation of the respiratory waveform in Tables 6, 7, and 8. From Tables 3 and 6, SMARS, Pos-Free Breath and WiRM are all not affected by phase noise. This is due to their design methodologies. Specifically, SMARS only utilises the energy of the CSI and does not consider phase. Pos-Free Breath computes the CSI-ratio to cancel out phase noise. WiRM employs conjugate-multiplied CSI data to cancel the noise. On the other hand, TR-BREATH does not contain any phase noise mitigation techniques and is thus affected.

The performance of the WiRM method in the face of multiplicative noise is shown in Tables 4 and 7. As seen, WiRM is particularly resilient to this type of noise thanks to

TABLE 2
Simulation parameters

Parameter Name	Value
Runtime	Time to generate 25 estimations
Antenna separation	0.05m
Transmitter-receiver separation	5m
Number of breaths	1
Complex amplitude ($\alpha_{T_a, R_b}(f)$)	$U([0.2, 2])^\dagger$
Breath amplitude ($\Delta d_{b, T_a, R_b}$)	$U([0.005, 0.01])^\ddagger$
Breath frequency BPM ($B_{Hz}(n)$)	15 BPM
Breath phase offset	0
Static component amplitude ($ H_{s, T_a, R_b} $)	$U([10, 20])$
Static component phase ($\angle H_{s, T_a, R_b}$)	$U([0, 2\pi])$
Dynamic component phase	$U([0, 2\pi])$
Dynamic component rotation direction	$U(\{-1, +1\})$

[†] $U(\mathcal{M})$ denotes a uniform distribution over the set \mathcal{M} .

[‡] These values correspond to phase angles close to $\pi/3$ following chest motion assumptions [29].

the use of both the magnitude and phase of the conjugate-multiplied CSI data. Note that multiplicative noise purely affects the magnitude of the CSI but not its phase. The BNR combining in Subsection 4.1.2 and the subcarrier combining in Subsection 4.2.3 simply rely on the phase of the CSI rather than the noise-affected magnitude. It is noteworthy that the other methods do not have this property and, as such, are greatly affected by multiplicative noise.

We note that all of the considered methods have superior performance on the simulated data than on the real-world dataset. While the simulated noise is always uncorrelated, white, and ideal, this is not always the case in the real world as the noise among antennas can potentially be correlated, or the noise may not necessarily be white. Additionally, for the purpose of simulation, the breath waveform is an ideal sinusoid with a fixed frequency of 15 BPM and there are no other movements in the simulated environment. This is unrealistic in a practical scenario as people breathe with varying waveforms, and there are often other movements in the room that may cause undue interference. Despite these differences, the simulated results still provide a useful metric for comparison of each method when examined under idealistic scenarios, allowing the impacts of certain classes of noise to be understood.

The simulation results show that the WiRM method consistently outperforms current state-of-the-art approaches across most categories, or achieves comparable performance where it does not. This observation confirms the robustness of WiRM against different types of noise.

TABLE 3
Respiratory Rate RMS Error (BPM): Phase Noise

Method	RMS Error (BPM)
WiRM	0.0
Pos-Free Breath	4.1
TR-BREATH	6.5
SMARS	0.8

TABLE 4
Respiratory Rate RMS Error (BPM): Multiplicative Noise

Std Dev	RMS Error (BPM)			
	WiRM	Pos-Free Breath	TR-BREATH	SMARS
0.1	0.0	0.0	0.3	5.5
0.25	0.0	0.9	0.5	12.7
0.5	0.0	5.0	0.3	17.4
0.75	0.0	7.7	0.3	18.0
1.0	0.0	7.5	0.3	17.7

TABLE 5
Respiratory Rate RMS Error (BPM): Thermal Noise

Std Dev	RMS Error (BPM)			
	WiRM	Pos-Free Breath	TR-BREATH	SMARS
0.1	0.0	0.0	0.4	0.8
0.5	0.0	0.0	1.1	0.8
1.0	0.0	0.0	2.4	1.9
5.0	2.6	7.1	7.7	13.3
10.0	5.6	7.7	7.0	17.5

TABLE 6
Respiratory Waveform Correlation ($|\rho|$): Phase Noise

Method	Correlation ($ \rho $)
WiRM	1.0
Pos-Free Breath	0.9

TABLE 7
Respiratory Waveform Correlation ($|\rho|$): Multiplicative Noise

Std Dev	Correlation ($ \rho $)	
	WiRM	Pos-Free Breath
0.1	1.0	1.0
0.25	1.0	0.9
0.5	1.0	0.4
0.75	1.0	0.0
1.0	1.0	0.0

TABLE 8
Respiratory Waveform Correlation ($|\rho|$): Thermal Noise

Std Dev	Correlation ($ \rho $)	
	WiRM	Pos-Free Breath
0.1	1.0	1.0
0.5	1.0	1.0
1.0	0.8	1.0
5.0	0.2	0.0
10.0	0.1	0.0

6 CONCLUSION

This paper has proposed a new method for the wireless monitoring of respiratory health using Wi-Fi CSI. Our solution has improved upon the accuracy of the current state-of-the-art respiratory rate estimation. We have demonstrated the effectiveness of applying a respiratory rate estimate to improve the performance of respiratory waveform estimation. We have also developed a simulation framework that enables a fair comparison of various respiration monitoring methodologies when subjected to different noise conditions.

REFERENCES

- [1] N. Kallioinen, A. Hill, M. J. Christofidis, M. S. Horswill, and M. O. Watson, "Quantitative systematic review: Sources of inaccuracy in manually measured adult respiratory rate data," *J. Adv. Nurs.*, vol. 77, no. 1, pp. 98–124, Jan. 2021.
- [2] P. Seddon, "Options for assessing and measuring chest wall motion," *Paediatric Respiratory Reviews*, vol. 16, no. 1, pp. 3–10, Jan. 2015.
- [3] X. Xu, J. Yu, Y. Chen, Y. Zhu, L. Kong, and M. Li, "BreathListener: Fine-grained breathing monitoring in driving environments utilizing acoustic signals," in *Proceedings of the 17th Annual International Conference on Mobile Systems, Applications, and Services*, ser. MobiSys '19. New York, NY, USA: Association for Computing Machinery, Jun. 2019, pp. 54–66.
- [4] H. Wan, S. Shi, W. Cao, W. Wang, and G. Chen, "RespTracker: Multi-user room-scale respiration tracking with commercial acoustic devices," in *IEEE INFOCOM 2021 - IEEE Conference on Computer Communications*, May 2021, pp. 1–10.
- [5] W. Mongan, R. Ross, I. Rasheed, Y. Liu, K. Ved, E. Anday, K. Dandekar, G. Dion, T. Kurzweg, and A. Fontecchione, "Data fusion of single-tag rfid measurements for respiratory rate monitoring," in *2017 IEEE Signal Processing in Medicine and Biology Symposium (SPMB)*, 2017, pp. 1–6.
- [6] C. Yang, X. Wang, and S. Mao, "Respiration monitoring with RFID in driving environments," *IEEE J. Sel. Areas Commun.*, vol. 39, no. 2, pp. 500–512, 2021.
- [7] A. Droitcour, V. Lubecke, J. Lin, and O. Boric-Lubecke, "A microwave radio for Doppler radar sensing of vital signs," in *2001 IEEE MTT-S International Microwave Symposium Digest (Cat. No.01CH37157)*, vol. 1, 2001, pp. 175–178 vol.1.
- [8] S. Yue, H. He, H. Wang, H. Rahul, and D. Katabi, "Extracting multi-person respiration from entangled RF signals," *Proc. ACM Interact. Mob. Wearable Ubiquitous Technol.*, vol. 2, no. 2, jul 2018. [Online]. Available: <https://doi.org/10.1145/3214289>
- [9] X. Liu, J. Cao, S. Tang, J. Wen, and P. Guo, "Contactless respiration monitoring via off-the-shelf WiFi devices," *IEEE Trans. Mob. Comput.*, vol. 15, no. 10, pp. 2466–2479, 2016.
- [10] P. Wang, B. Guo, T. Xin, Z. Wang, and Z. Yu, "TinySense: Multi-user respiration detection using Wi-Fi CSI signals," in *2017 IEEE 19th International Conference on E-Health Networking, Applications and Services (Healthcom)*, Oct. 2017, pp. 1–6.
- [11] F. Zhang, C. Wu, B. Wang, M. Wu, D. Bugos, H. Zhang, and K. J. R. Liu, "SMARS: Sleep monitoring via ambient radio signals," *IEEE Trans. Mob. Comput.*, vol. 20, no. 1, pp. 217–231, 2021.

- [12] C. Chen, Y. Han, Y. Chen, H.-Q. Lai, F. Zhang, B. Wang, and K. J. R. Liu, "TR-BREATH: Time-Reversal breathing rate estimation and detection," *IEEE Trans. Biomed. Eng.*, vol. 65, no. 3, pp. 489–501, 2018.
- [13] H. Zhuo, X. Wu, Q. Zhong, and H. Zhang, "Position-free breath detection during sleep via commodity WiFi," *IEEE Sens. J.*, vol. 23, no. 20, pp. 24 874–24 884, 2023.
- [14] N. Patwari, J. Wilson, S. Ananthanarayanan, S. K. Kasera, and D. R. Westenskow, "Monitoring breathing via signal strength in wireless networks," *IEEE Trans. Mob. Comput.*, vol. 13, no. 8, pp. 1774–1786, 2014.
- [15] C. Han, K. Wu, Y. Wang, and L. M. Ni, "WiFall: Device-free fall detection by wireless networks," in *IEEE INFOCOM 2014 - IEEE Conference on Computer Communications*, 2014, pp. 271–279.
- [16] F. Meneghello, D. Garlisi, N. D. Fabbro, I. Tinnirello, and M. Rossi, "SHARP: Environment and person independent activity recognition with commodity IEEE 802.11 access points," *IEEE Trans. Mob. Comput.*, vol. 22, no. 10, pp. 6160–6175, Oct. 2023.
- [17] C. Wu, F. Zhang, Y. Hu, and K. J. R. Liu, "GaitWay: Monitoring and recognizing gait speed through the walls," *IEEE Trans. Mob. Comput.*, vol. 20, no. 6, pp. 2186–2199, 2021.
- [18] F. Zhang, C. Chen, B. Wang, and K. J. R. Liu, "WiSpeed: A statistical electromagnetic approach for device-free indoor speed estimation," *IEEE Internet Things J.*, vol. 5, no. 3, pp. 2163–2177, 2018.
- [19] A. Dash, J. Gu, G. Wang, and N. Ansari, "Self-supervised learning for user localization," in *2024 International Conference on Computing, Networking and Communications (ICNC)*, Feb. 2024, pp. 886–890.
- [20] X. Zhang, Y. Gu, H. Yan, Y. Wang, M. Dong, K. Ota, F. Ren, and Y. Ji, "Wital: A COTS WiFi devices based vital signs monitoring system using NLOS sensing model," *IEEE Trans. Hum.-Mach. Syst.*, vol. 53, no. 3, pp. 629–641, Jun. 2023.
- [21] W.-H. Wang, B. Wang, X. Zeng, and K. J. Ray Liu, "WiResP: A robust Wi-Fi-based respiration monitoring via spectrum enhancement," *IEEE Sens. J.*, vol. 24, no. 13, pp. 20 999–21 011, 2024.
- [22] J. Gjengset, J. Xiong, G. McPhillips, and K. Jamieson, "Phaser: enabling phased array signal processing on commodity WiFi access points," in *Proceedings of the 20th Annual International Conference on Mobile Computing and Networking*, ser. *MobiCom '14*. New York, NY, USA: Association for Computing Machinery, 2014, p. 153–164. [Online]. Available: <https://doi.org/10.1145/2639108.2639139>
- [23] X. Wang, C. Yang, and S. Mao, "TensorBeat: Tensor decomposition for monitoring multi-person breathing beats with commodity WiFi," 2017. [Online]. Available: <https://arxiv.org/abs/1702.02046>
- [24] —, "PhaseBeat: Exploiting CSI phase data for vital sign monitoring with commodity WiFi devices," in *2017 IEEE 37th International Conference on Distributed Computing Systems (ICDCS)*, 2017, pp. 1230–1239.
- [25] Y. Zeng, D. Wu, R. Gao, T. Gu, and D. Zhang, "FullBreathe: Full human respiration detection exploiting complementarity of CSI phase and amplitude of WiFi signals," *Proc. ACM Interact. Mob. Wearable Ubiquitous Technol.*, vol. 2, no. 3, Sep. 2018. [Online]. Available: <https://doi.org/10.1145/3264958>
- [26] Y. Zeng, D. Wu, J. Xiong, J. Liu, Z. Liu, and D. Zhang, "MultiSense: Enabling multi-person respiration sensing with commodity WiFi," *Proc. ACM Interact. Mob. Wearable Ubiquitous Technol.*, vol. 4, no. 3, pp. 102:1–102:29, Sep. 2020.
- [27] X. Shen, L. Guo, Z. Lu, X. Wen, and Z. He, "WiRIM: Resolution improving mechanism for human sensing with commodity Wi-Fi," *IEEE Access*, vol. 7, pp. 168 357–168 370, 2019.
- [28] W. Xie, L. Gan, L. Huang, C. Shi, B. Liu, C.-H. Wu, Y.-T. Lee, J. Chen, and R. Zhang, "A real-time respiration monitoring system using WiFi sensing based on the concentric circle model," *IEEE Trans. Biomed. Circuits Syst.*, vol. 17, no. 2, pp. 157–168, 2023.
- [29] H. Wang, D. Zhang, J. Ma, Y. Wang, Y. Wang, D. Wu, T. Gu, and B. Xie, "Human respiration detection with commodity Wifi devices: Do user location and body orientation matter?" in *Proceedings of the 2016 ACM International Joint Conference on Pervasive and Ubiquitous Computing*, ser. *UbiComp '16*. New York, NY, USA: Association for Computing Machinery, Sep. 2016, pp. 25–36.
- [30] K. J. R. Liu and B. Wang, "Statistical principles of Time Reversal [perspectives]," *IEEE Signal Processing Magazine*, vol. 41, no. 1, pp. 31–37, 2024.
- [31] J. Wang, H. Du, D. Niyato, M. Zhou, J. Kang, and H. Vincent Poor, "Acceleration estimation of signal propagation path length changes for wireless sensing," *IEEE Transactions on Wireless Communications*, vol. 23, no. 9, pp. 11 476–11 492, 2024.
- [32] S. Khan, A. Alzaabi, Z. Iqbal, T. Ratnarajah, and T. Arslan, "A novel digital twin (DT) model based on WiFi CSI, signal processing and machine learning for patient respiration monitoring and decision-support," *IEEE Access*, vol. 11, pp. 103 554–103 568, 2023.
- [33] F. Abuhoureyah, K. S. Sim, and Y. Chiew Wong, "Multi-user human activity recognition through adaptive location-independent WiFi signal characteristics," *IEEE Access*, vol. 12, pp. 112 008–112 024, 2024.
- [34] K. Tsubota, Y. Nagatsu, and H. Hashimoto, "Biometric information acquisition system using VMD in Wi-Fi channel status information," in *IECON 2021 – 47th Annual Conference of the IEEE Industrial Electronics Society*, 2021, pp. 1–6.
- [35] A. Goldsmith, *Wireless Communications*. Cambridge University Press, 2005.
- [36] P. J. Schreier and L. L. Scharf, *Statistical Signal Processing of Complex-Valued Data: The Theory of Improper and Noncircular Signals*. Cambridge University Press, 2010.
- [37] L. R. Rabiner, R. W. Schafer, and C. M. Rader, "The chirp z-transform algorithm and its application," *The Bell System Technical Journal*, vol. 48, no. 5, pp. 1249–1292, 1969.
- [38] W. Heisenberg, "Über den anschaulichen inhalt der quantentheoretischen kinematik und mechanik," *Zeitschrift für Physik*, vol. 43, no. 3, pp. 172–198, Mar 1927. [Online]. Available: <https://doi.org/10.1007/BF01397280>
- [39] J. Allen and L. Rabiner, "A unified approach to short-time Fourier analysis and synthesis," *Proc. IEEE*, vol. 65, no. 11, pp. 1558–1564, 1977.
- [40] Q. Zhu, M. Chen, C.-W. Wong, and M. Wu, "Adaptive Multi-Trace Carving for robust frequency tracking in forensic applications," *IEEE Trans. Inf. Forensics Secur.*, vol. 16, pp. 1174–1189, 2021.
- [41] A. L. Goldberger, L. A. Amaral, L. Glass, J. M. Hausdorff, P. C. Ivanov, R. G. Mark, J. E. Mietus, G. B. Moody, C. K. Peng, and H. E. Stanley, "PhysioBank, PhysioToolkit, and PhysioNet: components of a new research resource for complex physiologic signals," *Circulation*, vol. 101, no. 23, pp. E215–20, Jun. 2000.
- [42] A. Cicone and H. Zhou, "Numerical analysis for Iterative Filtering with new efficient implementations based on FFT," Oct. 2018.
- [43] A. Cicone, S. Serra-Capizzano, and H. Zhou, "One or two frequencies? the Iterative Filtering answers," 2021. [Online]. Available: <https://arxiv.org/abs/2111.11741>
- [44] L. Lin, Y. Wang, and H. Zhou, "Iterative Filtering as an alternative algorithm for Empirical Mode Decomposition." *Advances in Adaptive Data Analysis*, vol. 1, pp. 543–560, 10 2009.
- [45] A. Stallone, A. Cicone, and M. Materassi, "New insights and best practices for the successful use of Empirical Mode Decomposition, Iterative Filtering and derived algorithms," *Sci. Rep.*, vol. 10, no. 1, p. 15161, Sep. 2020.
- [46] P. Hillyard, "rf_polysomnography_respiration_data_00," 2018. [Online]. Available: <https://doi.org/10.7910/DVN/X7AYXQ>